Archives of Biochemistry and Biophysics 550–551 (2014) 50–57

Contents lists available at ScienceDirect

Archives of Biochemistry and Biophysics

journal homepage: www.elsevier.com/locate/yabbi

Analysis of the solution structure of *Thermosynechococcus elongatus* photosystem I in *n*-dodecyl-*β*-D-maltoside using small-angle neutron scattering and molecular dynamics simulation

Rosemary K. Le [a], Bradley J. Harris [a], Ifeyinwa J. Iwuchukwu [a], Barry D. Bruce [b,c], Xiaolin Cheng [d,b], Shuo Qian [e], William T. Heller [e], Hugh O'Neill [e], Paul D. Frymier [a,c,*]

[a] Department of Chemical and Biomolecular Engineering, University of Tennessee, Knoxville, TN 37996, United States
[b] Department of Biochemistry and Cellular and Molecular Biology, University of Tennessee, Knoxville, TN 37996, United States
[c] Sustainable Energy Education and Research Center, University of Tennessee, Knoxville, TN 37996, United States
[d] Center for Molecular Biophysics, Oak Ridge National Laboratory, Oak Ridge, TN 37831, United States
[e] Biology and Soft Matter Division, Oak Ridge National Laboratory, Oak Ridge, TN 37831, United States

ARTICLE INFO

Article history:
Received 24 March 2014
Available online 24 April 2014

Keywords:
Small-angle neutron scattering
Membrane protein
Dummy-atom reconstruction
Detergent monolayer

ABSTRACT

Small-angle neutron scattering (SANS) and molecular dynamics (MD) simulation were used to investigate the structure of trimeric photosystem I (PSI) from *Thermosynechococcus elongatus* (*T. elongatus*) stabilized in *n*-dodecyl-*β*-D-maltoside (DDM) detergent solution. Scattering curves of detergent and protein–detergent complexes were measured at 18% D_2O, the contrast match point for the detergent, and 100% D_2O, allowing observation of the structures of protein/detergent complexes. It was determined that the maximum dimension of the PSI–DDM complex was consistent with the presence of a monolayer belt of detergent around the periphery of PSI. A dummy-atom reconstruction of the shape of the complex from the SANS data indicates that the detergent envelope has an irregular shape around the hydrophobic periphery of the PSI trimer rather than a uniform, toroidal belt around the complex. A 50 ns MD simulation model (a DDM ring surrounding the PSI complex with extra interstitial DDM) of the PSI–DDM complex was developed for comparison with the SANS data. The results suggest that DDM undergoes additional structuring around the membrane-spanning surface of the complex instead of a simple, relatively uniform belt, as is generally assumed for studies that use detergents to solubilize membrane proteins.

Introduction

Photosystem I (PSI)[1] is a large pigment protein complex involved in cyanobacterial, algal, and plant photosynthesis. PSI provides both a large antenna for harvesting solar energy and the reaction center that converts these excitons into a stable charge separation. It has been determined that PSI has an internal quantum yield near 1.0 [1]. The robust and stable nature of PSI has led to many studies using PSI in *in vitro* applications for alternative energy solutions, such as hydrogen or direct electricity production as part of biohybrid devices or materials [2–7].

In cyanobacteria, PSI is located in the thylakoid membrane and exists primarily as homo-trimeric complexes of the PSI monomer, a multi-subunit complex with several membrane-spanning domains [8]. The monomer of PSI from *Thermosynechococcus elongatus* (*T. elongatus*) is made up of 12 subunits. The PsaA and B subunits contain the majority of the transmembrane helices, the reaction center pigments including P700, ~100 light harvesting chlorophyll *a* (chl *a*), carotenoids, quinones, and the proximal iron–sulfur cluster (F_x) that functions as an electron acceptor [8,9]. The PsaC, D, and E subunits do not contain transmembrane domains yet are stably associated on the stromal surface of the thylakoid. The terminal electron acceptors, F_A and F_B are found in this stromal domain and coordinated via PsaC. Electrons are transferred from F_B to the soluble FeS protein, ferredoxin, upon its transient association with the PsaD and E subunits [10]. Ferredoxin then provides electrons to support carbon fixation and other redox reactions.

* Corresponding author at: Department of Chemical and Biomolecular Engineering, University of Tennessee, 419 Dougherty Engineering Building, Knoxville, TN 37996-2200, United States. Tel.: +1 865 974 4961 (O); Fax: +1 865 974 7076.
E-mail address: pdf@utk.edu (P.D. Frymier).

[1] *Abbreviations used:* SANS, small-angle neutron scattering; MD, molecular dynamics; PSI, photosystem I; *T. elongatus*, *Thermosynechococcus elongatus*; DDM, *n*-dodecyl-*β*-d-maltoside; chl *a*, chlorophyll *a*; F_x, proximal iron–sulfur cluster; CMC, critical micelle concentration; CSC, critical solubilization concentration; TEM, transmission electron microscopy; HFIR, High Flux Isotope Reactor; 2D, two-dimensional; R_g, radius of gyration; P(r), pair distance distribution function.

http://dx.doi.org/10.1016/j.abb.2014.04.005
0003-9861/

The monomer has an approximate diameter and height of 15 nm and 9 nm (Fig. 1A), respectively [11]. It was determined from the crystal structure of trimeric PSI from the thermophilic *T. elongatus* resolved at 2.5 Å [8] that the trimer has a clover-leaf-structure with a diameter of 22 nm (Fig. 1B) [12]. Hydrodynamic diameter measurements from dynamic light scattering of a single trimer have estimated its dimension to be 30 nm in diameter by 9 nm in height suggesting the presence of additional mass around the periphery of the complex that can be assumed to be lipid or detergent [13].

Since PSI is a large multi-subunit membrane complex its isolation requires the use of non-ionic detergents such as Triton X-100, *n*-octyl-*β*-D-glucoside, *n*-dodecyl-*β*-D-maltoside, or a combination of them. These detergents both disrupt the membrane and solubilize the membrane complexes in mixed micelles that prevent aggregation and mimic its native membrane-like environment. Though detergents allow membrane complexes to be soluble in aqueous solution, their abundance and non-native characteristics can interfere with the ability to study protein–protein interactions and/or structural and functional properties [13–15]. The difficulties associated with solubilizing and stabilizing membrane proteins like PSI are due primarily to the exposure of its hydrophobic domains, which are protected by the lipid bilayer in the native environment. Therefore it is necessary to understand the effects of detergents used for membrane protein studies, as it has been shown that short alkyl chain detergents are more effective at solubilization than long alkyl chain detergents, which can cause protein denaturation [16,17]. Furthermore, it is important to understand the impact of detergent micelles on membrane proteins in solution, particularly the protein–detergent interactions that affect protein conformation or cause aggregation. Recent studies [13,18] have shown that the critical micelle concentration (CMC) and critical solubilization concentration (CSC) are of particular importance for determining how effective a detergent is at solubilizing a membrane protein. Both parameters have been studied for various detergents, such as *n*-dodecyl-*β*-D-maltoside (DDM) which was used in this study.

Our interest in understanding the interaction of detergent with cyanobacterial PSI stems from its ability to undergo charge separation for unidirectional electron transfer upon exposure to light, which can be integrated into bio-hybrid solid-state electronic devices for electricity [19–23] or hydrogen [7,24–28] production. As these technologies have great potential in the field of energy conversion, it is important to develop robust, reproducible techniques to uniformly orient PSI molecules on conductive substrates or in complexes with other proteins. Knowledge of the protein–detergent interactions is important for retaining protein activity and preventing denaturing environments for studying protein function *in vitro* [29] as well as addressing issues related to solution-phase aggregation which could impact the oriented assembly of PSI at a surface.

Small-angle neutron scattering (SANS) is very useful for probing structural properties of biological complexes [30]. By varying the ratio of H_2O and D_2O in solution, which have distinct scattering length densities [31], it is possible to match the background scattering to one component of the complex, effectively masking it and allowing a view of the remaining portions of the complex without disturbing the complex. There have been many different applications of contrast matching methods, ranging from block copolymers [32,33] and self-assembled materials [34] to biological systems [35–37]. The naturally occurring differences in scattering length densities of protein and other molecules makes SANS with the contrast matching an excellent tool for such studies [38,39].

Molecular dynamics (MD) simulation is a valuable tool for interpreting neutron scattering data. It has been widely used to investigate polymer systems [40,41], chemical reactions [42–44], and biological systems [42–51]. Additionally, the simulations can be used to generate simulated scattering curves for comparison against experimental SANS data. This allows a greater understanding of the interactions between protein and detergent, and the structure of the overall complex. For example, Scott et al. demonstrated that MD models of membrane proteins, such as PSI, require additional bilayer lipid molecules beyond those defined in the crystal structure to maintain the native structure [52].

We combined neutron scattering and MD simulations to study the interaction of PSI from *T. elongatus* with DDM in solution to improve our understanding of how the complex is solubilized by the detergent. The results from MD simulations were compared to scattering from protein-detergent complexes with and without detergent contrast-matching, providing detailed structural information on the protein–detergent complex. The results indicate that the detergent belt around the PSI transmembrane domains is not consistent with a uniform toroidal structure, as previously suggested [18]. Instead, the monolayer of DDM molecules adopts a clover-like envelope around the PSI trimer shape. The structural insight gained not only improves the broader understanding of membrane protein–detergent interactions, but will also guide strategies for incorporating PSI into energy harvesting devices.

Materials and methods

Isolation and purification of trimeric PSI from T. elongatus

PSI trimers used in this study were obtained from *T. elongatus BP-1* [53]. Cells were grown in a bioreactor and stored at −80 °C

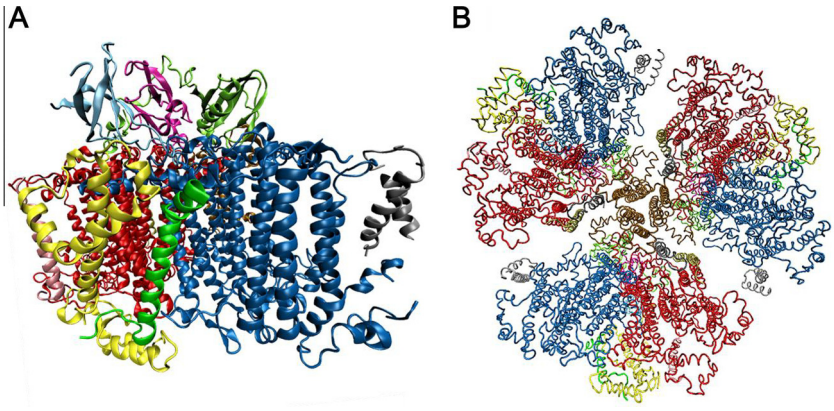

Fig. 1. (A) Crystal structure of *T. elongatus* PSI monomer (PDB ID: 1JB0) shown stromal side up. (B) Trimeric PSI complex constructed from 1JB0 structure shown lumenal side up.

until use for PSI preparation. Trimers were generated from frozen cell pellets following a protocol similar to that previously established by Fromme et al. [54]. Previous transmission electron microscopy (TEM) of the complexes purified in this manner also confirmed the uniformity and purity of the trimeric PSI nanoparticles [55]. Details of the growth and purification methods can be found in Iwuchukwu et al. [6,55]. Purified trimers were stored in 20 mM MES buffer with 0.03% DDM of 99.5% purity (GLYCON Biochemicals, D97002-C). The chl *a* concentration of the PSI trimer used was 0.59 mg/ml and 0.64 mg/ml in the 18% D_2O and 100% D_2O samples respectively.

Analytical procedures

The concentration of chlorophyll *a* present in the samples was determined by Eq. (1):

$$\frac{\mu g\ chl\ a}{ml} = Abs_{665} \times 13.9 \quad (1)$$

as in Hall (1999) [56]. The trimer concentration was approximated by stoichiometric conversion with conversion factors: 893 g chl *a* per mol chl *a*, 96 mol chl *a* per mol P_{700}, and 3 mol P_{700} per mol trimer.

Small-angle neutron scattering

SANS experiments were performed at the Bio-SANS beamline [57] located at the High Flux Isotope Reactor (HFIR) of the Oak Ridge National Laboratory. Samples were measured at 20 °C, in 1 mm path length quartz cells (Hellma U.S.A., Plainview, NY). Scattered neutrons were collected with a 1 m by 1 m two-dimensional (2D) position-sensitive detector with 192 by 192 pixel resolution (ORDELA, Inc, Oak Ridge, TN). The 2D data were corrected for detector pixel sensitivity, as well as the dark current, from ambient background radiation and the detector's electronic noise. The 2D reduced data were azimuthally averaged to yield the 1D scattering intensity $I(q)$ vs. q, where q is described by Eq. (2):

$$q = \frac{4\pi \sin(\theta)}{\lambda} \quad (2)$$

and 2θ is the scattering angle from the incident beam and λ is the neutron wavelength (6 Å, $\Delta\lambda/\lambda$, ≈0.15%). SANS data were taken at sample-to-detector distances of 1.1 m, 6.8 m, and 15.3 m for each sample to cover the expected q-range. The 1D profiles from different detector distances were merged to produce a complete scattering intensity plot.

PSI in 0.12% DDM was measured in 18% D_2O buffer, the contrast match point for the detergent [58], and in 100% D_2O buffer. Additionally, a PSI-free DDM solution at 0.12% (w/v) was measured in 100% D_2O. The corresponding buffers with DDM were also measured for background correction for the PSI-containing samples. The radius of gyration (R_g) was determined from the Guinier region of the SANS data with the Guinier approximation [59], Eq. (3):

$$I(q) = I(0)e^{\frac{q^2R_g^2}{3}} \quad (3)$$

where $I(0)$ is the forward scattering intensity, a shape-independent function of the total scattering power of the sample. A linear fit of $\ln(I(q))$ vs. q^2 (a Guinier plot) provides $I(0)$ and R_g from the y-intercept and slope, respectively [60]. The data were processed using the program package PRIMUS [61].

Shape restoration and MD simulation

The pair distance distribution function (P(r)) analysis of the SANS data was carried out using the indirect Fourier transform method implemented in GNOM [62]. The low-resolution shape of the scattering particles in solution was reconstructed using the *ab initio* modeling tool DAMMIF [63] and the SANS data from $q \leqslant 0.1$ Å^{-1}. The results of 50 runs of DAMMIF were averaged and the average structure from multiple runs using P3 symmetry for the trimeric complex [64] was determined using the program DAMAVER [65]. The program SUPCOMB [66] was used to compare the crystallographic structure of PSI (PDB ID: 1JB0) [8] with the model generated from the PSI–DDM SANS data collected in 18% D_2O, and to compare the model generated from the data in 100% D_2O with that generated from the PSI–DDM SANS data collected in 100% D_2O. The resulting overlaid structures were displayed using VMD [67] and rendered with Tachyon [68].

PSI/DDM models were developed and equilibrated using MD simulations for comparison to the SANS experimental data using the crystal structure of the PSI trimer from *T. elongatus* [69] as a starting point. For the first model (referred to as the DDM ring model), a toroidal ring of approximately 800 DDM molecules was built around the transmembrane region of the PSI trimer complex. A second model was created from this structure by adding an additional 200 DDM molecules into the voids within the PSI trimer in a bilayer-like configuration, forming a void filling sheet 5 nm in height, which is referred to as the void-filled DDM ring model. Simulations were performed using NAMD [70] with the CHARMM force field developed for biomolecular MD applications [71]. A set of CHARMM parameters for chlorophyll *a* (CHLA), beta carotene (BCR), and the iron–sulfur clusters (SF4), as well as DDM, were developed using previously published parameters from simulation studies of CHLA and BCR associated with PSII [72], SF4 from simulations of hydrogenase enzymes [73,74], and DDM [75]. MD simulations of the two models were equilibrated for approximately 5 ns in a water box using an isothermal–isobaric ensemble. Comparison of the SANS data with profiles calculated from the crystal structure and the results of MD simulations were performed using ORNL_SAS [76]. Analysis of the 5 ns equilibrated models revealed that the simulated ORNL_SAS profiles were nearly identical. Subsequently, a simulation of the void-filled DDM ring model was run for 50 ns and the experimental SANS data was compared against the profile calculated from the model. The MD trajectory of the 50 ns model was saved every 10,000 steps, resulting in 2500 frames for final analysis. All simulations were performed on the supercomputer Kraken [77] at The National Institute for Computational Sciences (NICS), co-located at the University of Tennessee – Knoxville and Oak Ridge National Laboratory campuses.

Results

SANS analysis of DDM micelles

SANS measurements were performed to characterize the DDM micelles in the absence of PSI. The SANS data P(r) derived from it are shown in Fig. 2A and D (red curve), respectively. The radius of gyration, R_g, of the DDM micelles in 100% D_2O was determined to be 2.04 ± 0.30 nm by the Guinier approximation (Fig. 3A) and 2.03 ± 0.02 nm from the P(r) fitting (Table 1). This result is consistent with the value of 2.01 nm determined by Abel et al. [78]. The fully extended length of a DDM molecule is ~2.3–2.8 nm, determined by Auer et al. [79], suggesting a reasonable micellar structure. The value of D_{max} from the GNOM fit is 6.4 nm, which is greater than twice this length and the P(r) is not symmetric, indicating that the micelles are not spherical. Using the gyration radius of 2.6 nm to determine the approximate surface area of a spherical DDM micelle (84.9 nm^2) and assuming a DDM monomer head has the projected area of an ellipse (0.63 nm^2, with a = 1.05 nm and b = 0.76 nm measured in PyMOL [80]) for dense hexagonal-packed

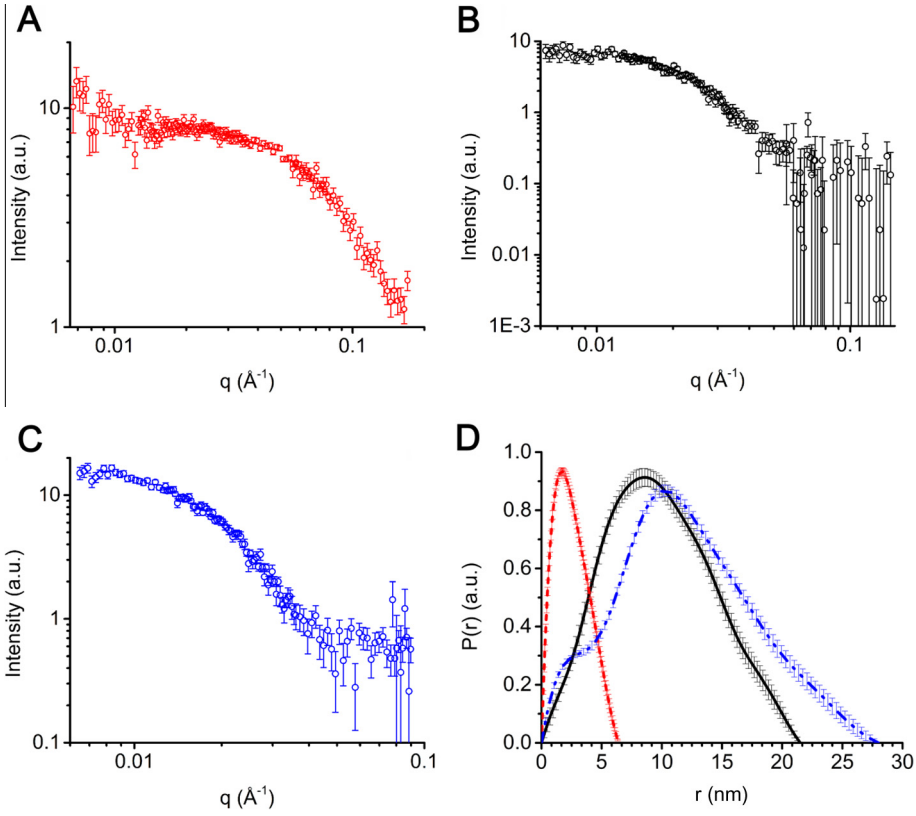

Fig. 2. Experimental scattering and particle distance distribution functions of SANS samples. (A) 0.12% DDM in 100% D_2O. (B) 0.12% DDM and PSI in 18% D_2O. (C) PSI in 100% D_2O. (D) P(r) of 0.12% (w/v) DDM in 100% D_2O (red curve), PSI with 0.12% (w/v) DDM in 18% D_2O (black curve), and PSI with 0.12% (w/v) DDM in 100% D_2O (blue curve) generated with GNOM. (For interpretation of the references to color in this figure legend, the reader is referred to the web version of this article.)

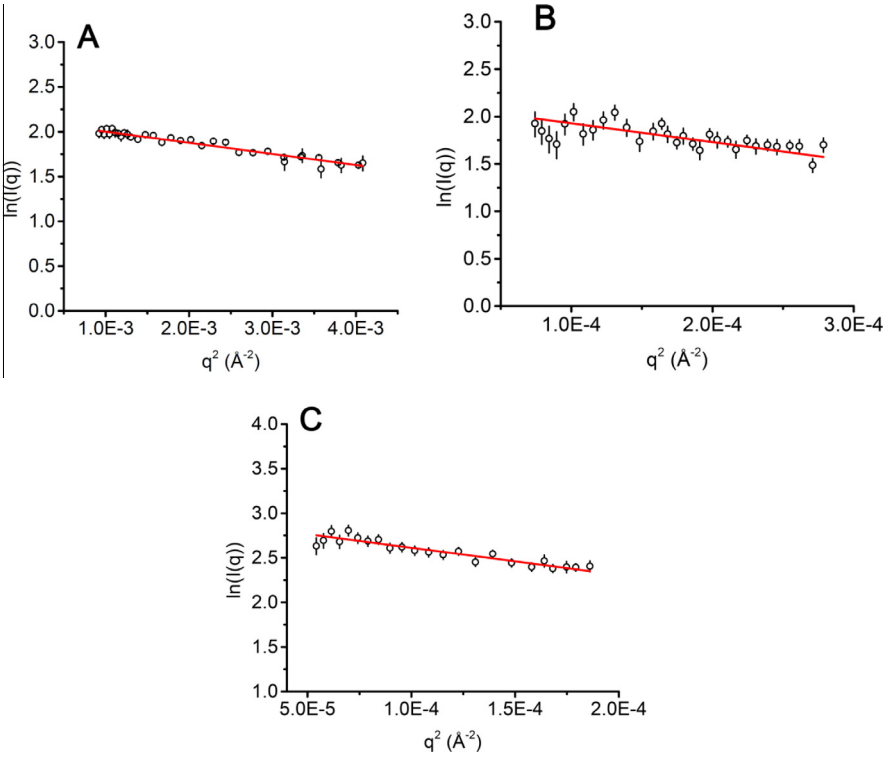

Fig. 3. Guinier analysis of (A) 0.12% (w/v) DDM in 100% D_2O, (B) PSI with 0.12% (w/v) DDM in 18% D_2O, (C) PSI with 0.12% (w/v) DDM in 100% D_2O shown with linear fits in the respective experimental scattering in the low-q regime with $qR_g < 1.3$. All plots are shown with the standard error associated with each point of the respective samples. See Table 1 for the resulting R_g values and associated error.

Table 1
Structural parameters of DDM micelles in 100% D_2O and PSI in 0.12% (w/v) DDM in 18% and 100% D_2O from SANS measurements. Calculated parameter values are shown as the mean value plus/minus the standard error of the mean of R_g.

Sample	[D_2O] (%)	[PSI trimer] (mM)	[DDM] (mM)	Guinier R_g (nm)	P(r) R_g (nm)	D_{max} (nm)
DDM only	100	0	2.35	2.04 ± 0.30	2.03 ± 0.02	6.4 ± 0.5
PSI+DDM	18	2.27×10^{-3}	2.35	7.79 ± 2.86	7.59 ± 0.09	21.5 ± 1.0
PSI+DDM	100	2.48×10^{-3}	2.35	9.49 ± 2.32	9.31 ± 0.11	28.0 ± 1.0

headgroups ($\eta = \frac{\pi}{2\sqrt{3}}$) yields an aggregation number of ~122 DDM molecules. Our measured aggregation number for the DDM micelles is consistent with previously reported values [81–87]. This aggregation number yields a micelle concentration of 1.79×10^{-2} mM (2.18 mM DDM in micelles) calculated from Eq. (4):

$$[\text{total detergent}] = [\text{monomer}] + [\text{micelles}] \times AN_{DDM} \quad (4)$$

where [total detergent] = 2.35 mM DDM, [monomer] = [CMC] = 0.17 mM DDM, and AN_{DDM} = 122 monomers per micelle.

SANS analysis of PSI

The SANS data collected for the PSI–DDM sample in 18% D_2O, the contrast match point for DDM, are shown in Fig. 2B and represent the scattering profile of PSI alone. The P(r) is shown in Fig. 2D. The R_g of PSI/DDM in 18% D_2O, presented in Table 1, are 7.79 ± 2.86 nm from Guinier analysis (Fig. 3B) and 7.59 ± 0.09 nm from P(r) fitting, and agree well with each other. The P(r) curve has an asymmetric shape similar to those previously reported for membrane proteins [75,76]. It has a peak at 8.6 nm and trails to a maximum particle size, D_{max} of 21.5 nm ± 1.0, suggesting a disk-shaped structure [14,88,89]. These dimensions are in good agreement with the crystal structure trimer (PDB ID: 1JB0) [8].

Interaction of PSI and DDM

The structure of the PSI–DDM complexes and the interactions between the two components of the mixture were probed by collecting scattering data for PSI with 0.12% (w/v) DDM in 100% D_2O, which is shown in Fig. 2C. At 100% D_2O there is maximum contrast between both PSI and DDM and the solvent and scattering results from both protein and detergent. The R_g of the protein–detergent complexes was determined by Guinier analysis (Fig. 3C) of the experimental scattering and by using the program GNOM, yielding R_g values of 9.49 ± 2.32 nm and 9.31 ± 0.11 nm, respectively. The P(r) curve has an asymmetric parabolic shape and peak at 10.1 nm that tapers off at longer distances, which is suggestive of a disk-like structure [14,90], a D_{max} of 28.0 ± 1.0 nm, and a shoulder feature at short vector lengths below 5 nm. In Table 1, the R_g value for PSI in 0.12% (w/v) DDM and 100% D_2O as determined by both Guinier analysis (9.49 ± 2.32 nm) and P(r) analysis (9.31 ± 0.11 nm) is larger than the value of a 7.7 nm in the DDM contrast-matched sample at 18% D_2O. A change in the D_{max} from PSI/DDM at 18% and 100% D_2O by 6.5 nm from P(r) is slightly larger than the expected size change for twice the fully extended length of a DDM molecule, approximately 5 nm. These values support the existence of detergent around the periphery of the trimer, surrounding the trans-membrane alpha-helixes that have also been seen in other studies [18,91–95].

The aggregation number for the PSI/DDM complex was estimated by assuming the complex is roughly a squat cylinder (made up of two concentric cylinders, the inner of which is PSI and the outer is a toroidal band of DDM) and that the DDM exists with the hydrophilic head groups closed packed on the periphery of the cylinder. The geometry of the cylinder was determined using the radius (13 nm) calculated from R_g of the PSI–DDM complex and a height excluding the stromal hump of 6.7 nm (height of the crystal structure of the PSI trimer transmembrane-spanning domain as measured by PyMOL). These radius and height values were used to calculate the approximate surface area of the periphery of a cylindrical PSI trimer-DDM complex (547 nm^2). The number of DDM monomer "heads" around the complex was determined by assuming a DDM monomer head has the projected area of an ellipse of 0.63 nm^2 (with axes of 1.05 nm and 0.76 nm as measured in PyMOL). It was further assumed that the monomer heads are packed in a dense hexagonal pattern around the periphery of the cylindrical complex ($\eta = \frac{\pi}{2\sqrt{3}}$). This procedure yields an aggregation number of ~792 DDM molecules per PSI trimer. The concentration of micelles was calculated using Eq. (5):

$$[\text{total detergent}] = [\text{monomer}] + [\text{PSI}] \times AN_{DDM-PSI} + [\text{micelles}] \times AN_{DDM} \quad (5)$$

where [total detergent] = 2.35 mM DDM, [monomer] = [CMC] = 0.17 mM DDM, [PSI] = 2.48×10^{-3} mM PSI trimer, $AN_{DDM-PSI}$ = 792 DDM monomers per trimer, and AN_{DDM} = 122 monomers per micelle. The resulting concentration of DDM complexed with PSI ([PSI] × $AN_{DDM-PSI}$) is 1.95 mM and that of detergent molecules in micelles ([micelles] × AN_{DDM}) is 0.23 mM. This yields a free micelle concentration of 1.85×10^{-3} mM. The free micelle concentration in the PSI–DDM sample was therefore about 10% of that in the DDM-only sample (1.79×10^{-2} mM free micelles). The resulting distribution of DDM monomer is 83% associated with PSI trimers, 10% in micelles, and 7% in non-associated monomer. For this reason, we used a monodisperse arbitrary particle model for calculating the distribution P(r) and, in the following simulations, modeled only the PSI/DDM complexes. This effectively assumes that the scattering due to the DDM micelles is negligible relative to that of the PSI/DDM complexes.

To visualize the structure of PSI in DDM, shape restoration was performed using DAMMIF from the SANS data for $q \leqslant 0.1$ $Å^{-1}$. The superposition of the average structure at 18% D_2O with the crystal structure can be seen in Fig. 4A–C. The reconstruction of PSI–DDM at 18% (green) appears to be slightly larger than the crystal structure (blue) due to the selected representation, but its D_{max} is ~22 nm, which is consistent with the expected diameter from the crystal structure. The reconstruction from the SANS data of the PSI–DDM complex in 100% D_2O (gray) shown in Fig. 4D–F overlaid with the model reconstructed from the SANS data collected in 18% D_2O (green) show where the DDM is found around the PSI structure. The models indicate that DDM exists primarily as a non-uniform envelope about the periphery of the trimer. The overall structure of the PSI–DDM complex provided by the reconstruction indicates that the DDM is localized around the periphery of the PSI (visible prominently in Fig. 4D–F) at each PSI monomer lobe and fills interstitial spaces between the monomers. There is little detergent on the stromal and lumenal surfaces, as can be seen in Fig. 4D–F. Examination of the surface characteristics of the stromal and lumenal surfaces of the crystal structure using VMD shows no significant hydrophobic patches on these surfaces, consistent with minimal coverage of detergent there. Examination of the transmembrane regions of the trimeric crystal structure revealed a uniform distribution of hydrophobic alpha-helices around the periphery of the complex, which is consistent with the distribution

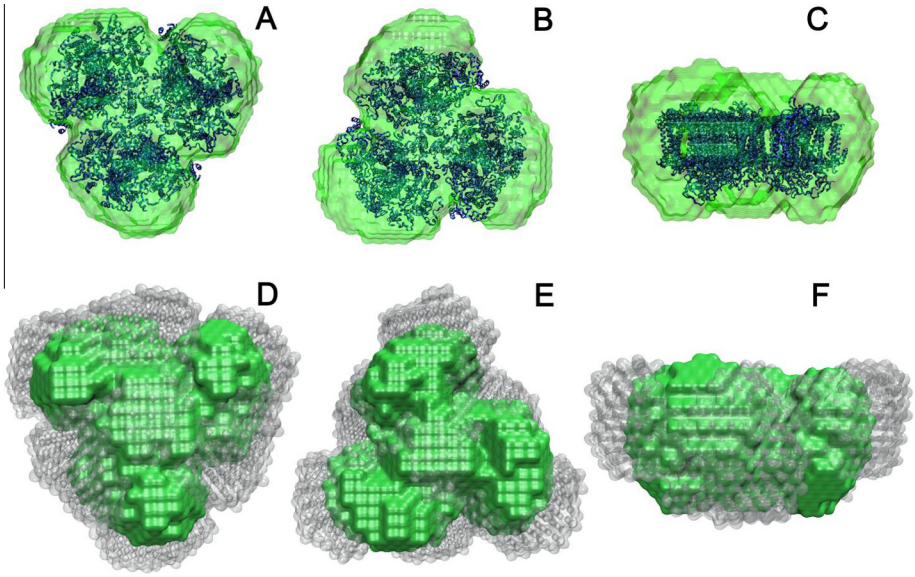

Fig. 4. Dummy-atom reconstruction of PSI trimer with DDM in 18% and 100% D_2O buffer using DAMMIF. (A), (B), (C) Stromal side up, lumenal side up, and side views of the trimeric crystal structure (blue) superimposed with the reconstruction of PSI–DDM at 18% D_2O (green), respectively. (D)–(F) Stromal side up, lumenal side up, and side views of PSI–DDM at 18% D_2O reconstruction (green) superimposed with PSI–DDM at 100% D_2O reconstruction (gray), respectively. (For interpretation of the references to color in this figure legend, the reader is referred to the web version of this article.)

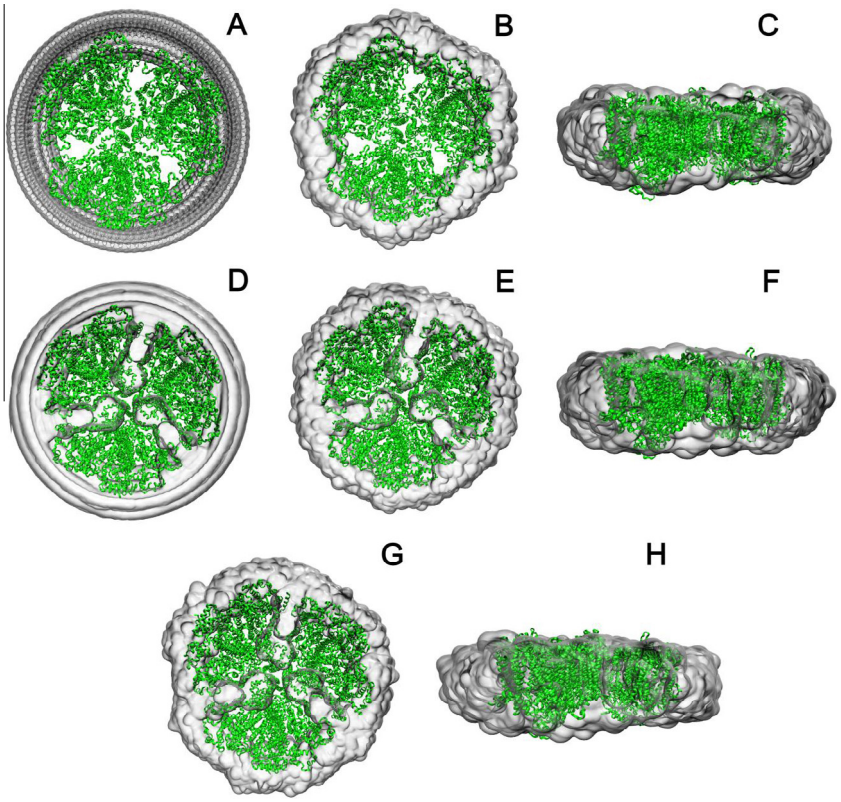

Fig. 5. NAMD generated configurations of (A) starting structure of PSI trimer in DDM ring, (B) PSI trimer in DDM ring after 5 ns equilibration, (C), side view of PSI trimer in DDM ring after 5 ns equilibration, (D) starting structure of PSI trimer in DDM ring with DDM in interstices of PSI trimer, (E) PSI trimer in DDM ring with DDM in interstices of PSI trimer after 5 ns equilibration, (F) side view of PSI trimer in DDM ring with DDM in interstices of PSI trimer after 5 ns equilibration, (G) PSI trimer in DDM ring with DDM in interstices of PSI trimer after 50 ns equilibration, and (H) side view of PSI trimer in DDM ring with DDM in interstices of PSI trimer after 50 ns equilibration. All views are shown with the lumenal side of protein complex facing up.

of detergent molecules within the interstitial spaces of the monomers and on the exposed outer surfaces.

Atomic-resolution PSI/DDM models were developed and equilibrated using MD simulations for comparison to the SANS experimental data. The starting structure of the DDM ring model and the void-filled DDM ring model can be seen in Fig. 5A and D, respectively. After 5 ns of equilibration for each of the models, the detergent molecules evolved to a less uniform belt around

the protein and detergent molecules began to move into the interstitial spaces between the monomers (not shown). The resulting equilibrated structures were then used to generate theoretical scattering curves using ORNL_SAS for comparison with the SANS data. The model profiles calculated from the two 5 ns-equilibrated models were nearly identical when superimposed (not shown). Due to the near identity of the two models, the void-filled model was used for a subsequent 50 ns equilibration. The averaged RMSD of the C-alphas of each PSI monomer generated from the simulation starting structure for the void-filled model after 50 ns is shown in Fig. 6.

The quality of the fit of the final model and the degree to which the "monolayer belt" model contributes to the calculated SANS profile can be seen in Fig. 7. Fitting the theoretical scattering curve of only the crystal structure trimer of PSI (PDB ID: 1JB0) (Fig. 7, green curve) yields a χ^2 value of 8.85, compared to $\chi^2 = 3.83$ for the final void-filled PSI–DDM model (red curve). This result supports the requirement of reconstructing the PSI trimer complex with detergent around the membrane-spanning domains to account for the increase in particle diameter indicated by the measured SANS data. Taken together with the DAMMIF reconstruction (Fig. 4D–F), the results suggest that the idealized geometry of the detergent ring encapsulating the hydrophobic regions of the protein used as the starting point for the simulations is a simplification that does not fully represent the interaction of DDM with PSI trimers. It should be noted that the modeled belt of detergent has become less uniformly distributed around PSI as the simulation progressed in time (compare Fig. 5E and F with G and H). With longer simulations the non-uniformity could develop into a more lobed structure, with the detergent concentrated around the lobes of PSI, giving a larger maximum diameter.

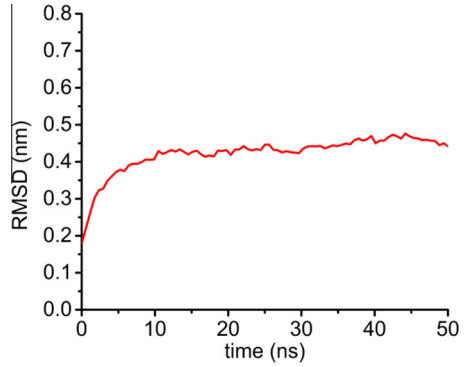

Fig. 6. C-alpha RMSD values versus time of void-filled model simulation after 50 ns. This curve was generated from the simulation starting structure.

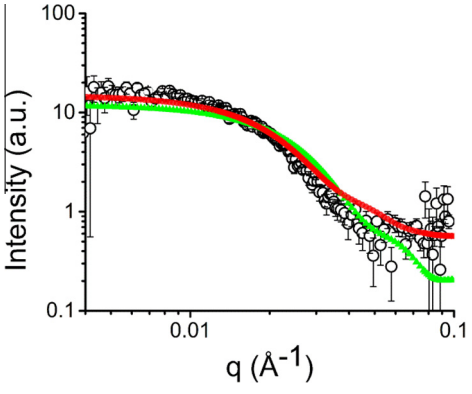

Fig. 7. Comparison of PSI/DDM in 100% D_2O experimental scattering data (black) and ORNL_SAS fit simulation of NAMD constructed void-filled DDM ring model (red). The trimeric crystal structure of PSI (PDB ID: 1JB0) was fit for comparison to theoretical scattering of the model reconstruction (green). (For interpretation of the references to color in this figure legend, the reader is referred to the web version of this article.)

Conclusions

The solution structure of detergent-associated PSI preparations was investigated by SANS analysis and produced results that have not been seen previously. Analysis and modeling of the data with and without the scattering contribution of DDM suggests that the detergent exists primarily as a belt surrounding the transmembrane domains of the protein complex. To explore this further, atomistic MD simulations of a DDM detergent-PSI model were performed. The SANS profiles calculated from the resulting models demonstrate that the inclusion of a detergent belt around PSI results in a structure more consistent with the experimental data but indicate that the models fail to reproduce key structural features of the DDM distribution around the protein complex. This study provides important insights into properties of PSI from the thermophile *T. elongatus* in solution with detergent that can be utilized in designing solutions possessing minimal aggregation for energy converting applications that could lead to enhanced operation and longer useful lifetimes. Additionally, the results provide new information about how detergent surrounds membrane proteins, which will be key for understanding how these detergent/protein complexes can interact with other proteins or surfaces to form conjugate structures for energy applications, such as protein fusions [7,26,96] or surface attachments [20–22,97]. The often-seen schematics of membrane proteins suspended in solution within a uniform detergent structure are an idealization and oversimplification, as the results presented here demonstrate.

Author contributions

The manuscript was written through contributions of all authors. All authors have given approval to the final version of the manuscript.

Acknowledgments

The authors would like to acknowledge financial support for Rosemary Le and Ifeyinwa Iwuchukwu from the National Science Foundation's IGERT program (DGE-0801470), Bradley Harris from the NSF-EPSCoR sponsored TN-SCORE (NSF EPS-1004083) and the University of Tennessee Sustainable Energy Education and Research Center (SEERC) for materials. HON acknowledges the support of Photosynthetic Antenna Research Center (PARC), an Energy Frontier Research Center funded by the U.S. Department of Energy, Office of Science, Office of Basic Energy Sciences under Award Number DE-SC 0001035. The Center for Structural Molecular Biology operates BioSANS and is supported by the U.S. DOE, Office of Science, Office of Biological and Environmental Research Project ERKP291. The High Flux Isotope Reactor is sponsored by the Scientific User Facilities Division, Basic Energy Sciences. Oak Ridge National Laboratory (ORNL) is managed by UT-Battelle, LLC, for the U.S. Department of Energy (DOE) under contract No. DE-AC05-00OR22725.

This material is based upon work supported by the National Science Foundation under Grant numbers 0711134, 0933959, 1041709, and 1041710 and the University of Tennessee through the use of the Kraken computing resource at the National Institute for Computational Sciences (http://www.nics.tennessee.edu).

References

[1] N. Nelson, J. Nanosci. Nanotechnol. 9 (3) (2009) 1709–1713.
[2] A. Badura, B. Esper, K. Ataka, C. Grunwald, C. Wöll, J. Kuhlmann, J. Heberle, M. Rögner, Photochem. Photobiol. 82 (5) (2006) 1385–1390.
[3] H. Krassen, A. Schwarze, B.R. Friedrich, K. Ataka, O. Lenz, J. Heberle, ACS Nano 3 (12) (2009) 4055–4061.
[4] P.N. Ciesielski, D.E. Cliffel, G.K. Jennings, J. Phys. Chem. A 115 (15) (2011) 3326–3334.
[5] G.D. Scholes, G.R. Fleming, A. Olaya-Castro, R. van Grondelle, Nat. Chem. 3 (10) (2011) 763–774.
[6] I.J. Iwuchukwu, E. Iwuchukwu, R. Le, C. Paquet, R. Sawhney, B. Bruce, P. Frymier, Int. J. Hydrogen Energy 36 (18) (2011) 11684–11692.
[7] C.E. Lubner, R. Grimme, D.A. Bryant, J.H. Golbeck, Biochemistry 49 (3) (2009) 404–414.
[8] P. Jordan, P. Fromme, H.T. Witt, O. Klukas, W. Saenger, N. Krausz, Nature 411 (6840) (2001) 909–917.
[9] J.H. Golbeck, Annu. Rev. Plant Physiol. Plant Mol. Biol. 43 (1) (1992) 293–324.
[10] A.L. Zilber, R. Malkin, Plant Physiol. 99 (3) (1992) 901–911.
[11] R.C. Ford, A. Holzenburg, EMBO J. 7 (8) (1988) 2287–2293.
[12] I. Grotjohann, P. Fromme, Photosynth. Res. 2005 (2005) 51.
[13] D. Mukherjee, M. May, B. Khomami, J. Colloid Interface Sci. 358 (2) (2011) 477–484.
[14] H. O'Neill, W.T. Heller, K.E. Helton, V.S. Urban, E. Greenbaum, J. Phys. Chem. B 111 (16) (2007) 4211–4219.
[15] P. Thiyagarajan, D.M. Tiede, J. Phys. Chem. 98 (40) (1994) 10343–10351.
[16] H. Hauser, Biochim. Biophys. Acta (BBA) – Biomembr. 1508 (1–2) (2000) 164–181.
[17] R.M. Garavito, S. Ferguson-Miller, J. Biol. Chem. 276 (35) (2001) 32403–32406.
[18] F. Müh, A. Zouni, Biochim. Biophys. Acta (BBA) – Biomembr. 1778 (10) (2008) 2298–2307.
[19] R. Das, P.J. Kiley, M. Segal, J. Norville, A.A. Yu, L. Wang, S.A. Trammell, L.E. Reddick, R. Kumar, F. Stellacci, N. Lebedev, J. Schnur, B.D. Bruce, S. Zhang, M. Baldo, Nano Lett. 4 (6) (2004) 1079–1083.
[20] C.J. Faulkner, S. Lees, P.N. Ciesielski, D.E. Cliffel, G.K. Jennings, Langmuir 24 (16) (2008) 8409–8412.
[21] P.N. Ciesielski, F.M. Hijazi, A.M. Scott, C.J. Faulkner, L. Beard, K. Emmett, S.J. Rosenthal, D. Cliffel, Bioresour. Technol. 101 (9) (2010) 3047–3053.
[22] G. LeBlanc, G. Chen, G.K. Jennings, D.E. Cliffel, Langmuir 28 (21) (2012) 7952–7956.
[23] A. Mershin, K. Matsumoto, L. Kaiser, D. Yu, M. Vaughn, M.K. Nazeeruddin, B.D. Bruce, M. Graetzel, S. Zhang, Sci. Rep. (2012) 2.
[24] R.A. Grimme, C.E. Lubner, D.A. Bryant, J.H. Golbeck, J. Am. Chem. Soc. 130 (20) (2008) 6308–6309.
[25] R.A. Grimme, C.E. Lubner, J.H. Golbeck, Dalton Trans. 45 (2009) 10106–10113.
[26] C.E. Lubner, A.M. Applegate, P. Knörzer, A. Ganago, D.A. Bryant, T. Happe, J.H. Golbeck, Proc. Natl. Acad. Sci. U.S.A. 108 (52) (2011) 20988–20991.
[27] M. Ihara, H. Nishihara, K.S. Yoon, O. Lenz, B. Friedrich, K. Nakamoto, K. Kojima, D. Honma, T. Kamachi, I. Okura, Photochem. Photobiol. 82 (2006) 676.
[28] L.M. Utschig, N.M. Dimitrijevic, O.G. Poluektov, S.D. Chemerisov, K.L. Mulfort, D.M. Tiede, J. Phys. Chem. Lett. 2 (3) (2011) 236–241.
[29] P. Kiley, X. Zhao, M. Vaughn, M.A. Baldo, B.D. Bruce, S. Zhang, PLoS Biol. 3 (7) (2005) e230.
[30] W.T. Heller, Acta Crystallogr. Sect. D-Biol. Crystallogr. 66 (2010) 1213–1217.
[31] D.I. Svergun, M.H.J. Koch, Curr. Opin. Struct. Biol. 12 (5) (2002) 654–660.
[32] S. Forster, E. Wenz, P. Lindner, Phys. Rev. Lett. 77 (1996) 95.
[33] G.A. McConnell, E.K. Lin, A.P. Gast, J.S. Huang, M.Y. Lin, S.D. Smith, Faraday Discuss. (1994) 121.
[34] H. Bagger Jorgensen, U. Olsson, K. Mortensen, Langmuir 13 (1997) 1413.
[35] J. Gau-Racine, J. Lal, M. Zeghal, L. Auvray, J. Phys. Chem. B 111 (2007) 9900.
[36] K.J. Mutch, J.S. van Duijneveldt, J. Eastoe, I. Grillo, R.K. Heenan, Langmuir 24 (2008) 3053.
[37] U.S. Jeng, T.L. Lin, J.M. Lin, D.L. Ho, Phys. B: Condens. Matter 385–386 (2006) 865.
[38] S. Qian, R. Dean, V.S. Urban, B.N. Chaudhuri, PLoS ONE 7 (12) (2012) e52690.
[39] E.P. Gogol, D.M. Engelman, Biophys. J . 46 (4) (1984) 491–495.
[40] G.S. Grest, K. Kremer, Phys. Rev. A 33 (5) (1986) 3628–3631.
[41] K. Kremer, G.S. Grest, J. Chem. Phys. 92 (1990) 5057.
[42] M. Tuckerman, K. Laasonen, M. Sprik, M. Parrinello, J. Chem. Phys. 103 (1995) 150.
[43] A.K. Rappe, W.A. Goddard III, J. Phys. Chem. 95 (8) (1991) 3358–3363.
[44] D. Borgis, J.T. Hynes, J. Chem. Phys. 94 (1991) 3619.
[45] M. Karplus, G.A. Petsko, Nature 347 (6294) (1990) 631–639.
[46] M. Karplus, J.A. McCammon, Nat. Struct. Mol. Biol. 9 (9) (2002) 646–652.
[47] M. Karplus, J. Kuriyan, Proc. Natl. Acad. Sci. U.S.A. 102 (19) (2005) 6679–6685.
[48] J.A. McCammon, B.R. Gelin, M. Karplus, Nature 267 (5612) (1977) 585–590.
[49] A.D. MacKerell, D. Bashford, M. Bellott, R.L. Dunbrack, J.D. Evanseck, M.J. Field, S. Fischer, J. Gao, H. Guo, S. Ha, D. Joseph-McCarthy, L. Kuchnir, K. Kuczera, F.T.K. Lau, C. Mattos, S. Michnick, T. Ngo, D.T. Nguyen, B. Prodhom, W.E. Reiher, B. Roux, M. Schlenkrich, J.C. Smith, R. Stote, J. Straub, M. Watanabe, J. Wiórkiewicz-Kuczera, D. Yin, M. Karplus, J. Phys. Chem. B 102 (18) (1998) 3586–3616.
[50] A.D. Mackerell, J. Comput. Chem. 25 (13) (2004) 1584–1604.
[51] D.L. Beveridge, F.M. DiCapua, Annu. Rev. Biophys. Biophys. Chem. 18 (1) (1989) 431–492.
[52] S.P. Scott, K.M. Amy, R.B. David, J.S. James, A.L. Cynthia, M.H. Margaret, Applications of Molecular Modeling to Challenges in Clean Energy, vol. 1133, American Chemical Society, 2013, pp. 177–202.
[53] Y. Nakamura, T. Kaneko, S. Sato, M. Ikeuchi, H. Katoh, S. Sasamoto, A. Watanabe, M. Iriguchi, K. Kawashima, T. Kimura, Y. Kishida, C. Kiyokawa, M. Kohara, M. Matsumoto, A. Matsuno, N. Nakazaki, S. Shimpo, M. Sugimoto, C. Takeuchi, M. Yamada, S. Tabata, DNA Res. 9 (4) (2002) 123–130.
[54] P. Fromme, H.T. Witt, Biochim. Biophys. Acta (BBA) – Biomembr. 1365 (1–2) (1998) 175–184.
[55] I.J. Iwuchukwu, M. Vaughn, N. Myers, H. O'Neill, P. Frymier, B.D. Bruce, Nat. Nanotechnol. 5 (1) (2010) 73–79.
[56] D.O. Hall, K.K. Rao, Photosynthesis, sixth ed., Cambridge University Press, New York, 1999.
[57] G.W. Lynn, W. Heller, V. Urban, G.D. Wignall, K. Weiss, D.A.A. Myles, Phys. B: Condens. Matter 385–386 (2006) 880–882. Part 2 (0).
[58] P.A. Timmins, M. Leonhard, H.U. Weltzien, T. Wacker, W. Welte, FEBS Lett. 238 (2) (1988) 361–368.
[59] A. Guinier, G. Fournet, *Small-Angle Scattering of X-Rays*, 1955.
[60] D.A. Jacques, J. Trewhella, Protein Sci. 19 (4) (2010) 642–657.
[61] P.V. Konarev, V.V. Volkov, A.V. Sokolova, M.H.J. Koch, D.I. Svergun, J. Appl. Crystallogr. 36 (5) (2003) 1277–1282.
[62] D.I. Svergun, J. Appl. Crystallogr. 25 (1992) 495.
[63] D. Franke, D.I. Svergun, J. Appl. Cryst. 42 (2009) 342–346.
[64] M. Rowicka, A. Kudlicki, Z. Otwinowski, Acta Crystallogr. Sect. 58 (6) (2002) 574–579.
[65] V.V. Volkov, D.I. Svergun, J. Appl. Crystallogr. 36 (2003) 860–864 (3 Part 1).
[66] M.B. Kozin, D.I. Svergun, J. Appl. Crystallogr. 34 (1) (2001) 33–41.
[67] W. Humphrey, A. Dalke, K. Schulten, J. Mol. Graph. 14 (1996) 33–38.
[68] J. Stone, An Efficient Library for Parallel Ray Tracing and Animation, Computer Science Department, University of Missouri-Rolla, 1998.
[69] P. Fromme, P. Jordan, N. Krauss, Biochim. Biophys. Acta Bioenerg. 1507 (1–3) (2001) 5–31.
[70] M.T. Nelson, W. Humphrey, A. Gursoy, A. Dalke, L.V. Kale, R.D. Skeel, K. Schulten, Int. J. Supercomput. Appl. High Perform. Comput. 10 (4) (1996) 251–268.
[71] B.R. Brooks, C.L. Brooks, A.D. Mackerell, L. Nilsson, R.J. Petrella, B. Roux, Y. Won, G. Archontis, C. Bartels, S. Boresch, A. Caflisch, L. Caves, Q. Cui, A.R. Dinner, M. Feig, S. Fischer, J. Gao, M. Hodoscek, W. Im, K. Kuczera, T. Lazaridis, J. Ma, V. Ovchinnikov, E. Paci, R.W. Pastor, C.B. Post, J.Z. Pu, M. Schaefer, B. Tidor, R.M. Venable, H.L. Woodcock, X. Wu, W. Yang, D.M. York, M. Karplus, J. Comput. Chem. 30 (10) (2009) 1545–1614.
[72] L. Zhang, D.A. Silva, Y.J. Yan, X.H. Huang, J. Comput. Chem. 33 (25) (2012) 1969–1980.
[73] C.H. Chang, K. Kim, J. Chem. Theory Comput. 5 (4) (2009) 1137–1145.
[74] D.M.A. Smith, Y.J. Xiong, T.P. Straatsma, K.M. Rosso, T.C. Squier, J. Chem. Theory Comput. 8 (6) (2012) 2103–2114.
[75] S. Abel, F.Y. Dupradeau, E.P. Raman, A.D. MacKerell, M. Marchi, J. Phys. Chem. B 115 (3) (2011) 487–499.
[76] E. Tjioe, W.T. Heller, J. Appl. Crystallogr. 40 (4) (2007) 782–785.
[77] M.R. Fahey, L. Crosby, G. Rogers, V. Hazlewood, in: J. Vetter (Ed.), Contemporary High Performance Computing: from Petascale Toward Exascale, Taylor and Francis, Boca Raton, 2013, pp. 453–491.
[78] S.p. Abel, F.o.-Y. Dupradeau, E.P. Raman, A.D. MacKerell, M. Marchi, J. Phys. Chem. B 115 (3) (2010) 487–499.
[79] M. Auer, G.A. Scarborough, W. Kuhlbrandt, Nature 392 (6678) (1998) 840–843.
[80] Schrodinger, LLC, The PyMOL Molecular Graphics System, Version 1.3r1. 2010.
[81] T. Vanaken, S. Foxall-Vanaken, S. Castleman, S. Ferguson-Miller, in: B.F. Sidney Fleischer (Ed.), Methods in Enzymology, vol. 125, Academic Press, 1986, pp. 27–35.
[82] L.-A. Barret, C. Barrot-Ivolot, S. Raynal, C. Jungas, A. Polidori, F. Bonneté, J. Phys. Chem. B 117 (29) (2013) 8770–8781.
[83] C. Dupuy, X. Auvray, C. Petipas, I. Rico-Lattes, A. Lattes, Langmuir 13 (15) (1997) 3965–3967.
[84] C. Tanford, The Hydrophobic Effect: Formation of Micelles and Biological Membranes, second ed., J. Wiley and Sons, New York, 1980.
[85] J. Lipfert, L. Columbus, V.B. Chu, S.A. Lesley, S. Doniach, J. Phys. Chem. B 111 (43) (2007) 12427–12438.
[86] P. Strop, A.T. Brunger, Protein Sci. 14 (8) (2005) 2207–2211.
[87] J. Lipfert, L. Columbus, V.B. Chu, S.A. Lesley, S. Doniach, J. Phys. Chem. B 111 (2007) 12427.
[88] X.G. Hong, Y.X. Weng, M. Li, Biophys. J. 1082 (2004) 86.
[89] M.G. Santonicola, A.M. Lenhoff, E.W. Kaler, Biophys. J. 94 (2008) 3647.
[90] R.M. Stroud, D.A. Agard, Biophys. J . 25 (3) (1979) 495–512.
[91] M. le Maire, P. Champeil, J.V. Moller, Biochim. Biophys. Acta Biomembr. 1508 (2000) 86.
[92] J.V. Moller, M. Lemaire, J. Biol. Chem. 268 (1993) 18659.
[93] M. Roth, A. Lewit-Bentley, H. Michel, J. Deisenhofer, R. Huber, D. Oesterhelt, Nature 340 (6235) (1989) 659–662.
[94] E. Pebaypeyroula, R.M. Garavito, J.P. Rosenbusch, M. Zulauf, P.A. Timmins, Structure 1051 (1995) 3.
[95] M. Ceccarelli, M. Marchi, J. Phys. Chem. B 107 (2003) 1423.
[96] M. Ihara, H. Nakamoto, T. Kamachi, I. Okura, M. Maeda, Photochem. Photobiol. 82 (2006) 1677.
[97] P.N. Ciesielski, A.M. Scott, C.J. Faulkner, B.J. Berron, D.E. Cliffel, G.K. Jennings, ACS Nano 2 (12) (2008) 2465–2472.